Structural and Multidisciplinary Optimization (2023) 66:27
https://doi.org/10.1007/s00158-022-03436-1

RESEARCH PAPER

The connection between digital-twin model and physical space for rotating blade: an atomic norm-based BTT undersampled signal reconstruction method

Ruochen Jin[1] · Laihao Yang[1] · Zhibo Yang[1] · Yu Sun[1] · Zhu Mao[2] · Ruqiang Yan[1] · Xuefeng Chen[1]

Received: 1 June 2022 / Revised: 10 October 2022 / Accepted: 14 October 2022 / Published online: 11 January 2023

Abstract
Digital twin that shows great potential in different fields may serve as the enabling technology for the health monitoring of aero-engine blade. However, due to the harsh conditions inside the aero-engine, one of the most challenging issues for the implementation of digital-twin-based blade health monitoring is the lack of an accurate connection method between the digital-twin model and the physical entity for rotating blade. Wherein, the key is how to measure the blade data accurately. The emerging blade tip timing (BTT), an effective non-contact measurement method for blades, has received extensive attention recently. Whereas, due to the limited probes that are allowed to be installed on the engine casing, the BTT signal is generally incomplete and under-sampling, which makes it very difficult to reconstruct the blade vibration parameters from the measured data. In this study, a novel paradigm for blade vibration parameter reconstruction with super-resolution from the undersampled BTT signal is proposed based on atomic norm soft thresholding (AST), which may offer accurate blade vibration information for the construction and updating of blade digital-twin model. Unlike the conventional reconstruction method that generally needs the interested signal to be sparse under a finite discrete dictionary for successful reconstruction, the proposed AST-based blade vibration parameter reconstruction method can take any continuous value in the frequency domain from the measurement data with fewer sampling numbers and higher under-sampling rate. Both numerical simulation and experimental verification are utilized to verify the validity of the proposed method. The comparative results indicate that the proposed method performs well in resisting "incomplete." Meanwhile, the proposed method performs better than state-of-the-art methods under conditions with fewer data.

Keywords blade tip timing · Atomic norm · Gridless · Frequency estimation · Digital twin

1 Introduction

Rotor blade is an important component that affects the performance and safety of aero-engine, and it is prone to crack damage, fatigue fracture, and other faults in the harsh service environment such as foreign object damage, aerodynamic excitation, high temperature, etc. (Mohamed et al. 2019; Yang et al. 2022). The crack damage will further propagate and finally lead to the fracture of the blade, causing a severe accident (Yang et al. 2021a, c; Yang et al. 2021b). Therefore, it is of great significance to monitor and diagnose the crack of the aero-engine rotor blade. Structural health monitoring (SHM), as a time-scale measurement method to diagnose and control important points in the structure (Farrar and Worden 2010), has been widely used in the fields of surface defect detection (Abbas and Shafiee 2018) and crack damage identification (Witos 2013). However, at present, the

Responsible Editor: Chao Hu

Topical Collection: Advanced Optimization Enabling Digital Twin Technology.
Guest Editors: C. Hu, V. A. Gonzalez, T. Kim, O. San, Z. Hu, P. Zheng

✉ Laihao Yang
yanglaihao@xjtu.edu.cn

[1] The State Key Laboratory for Manufacturing Systems Engineering, Xi'an Jiaotong University, Xi'an 710049, People's Republic of China

[2] The Mechanical and Materials Engineering Department, Worcester Polytechnic Institute, Worcester, MA 01609-2280, USA

SHM technology often suffers from the following problems: inapplicable model, incomplete data, and insufficient virtual-real interaction, so it is difficult to be directly applied to the condition monitoring of aero-engine rotor blades. Specifically, it includes:

(1) Traditional blade crack monitoring methods mainly rely on deterministic modeling, where the parameters are difficult to follow the changes in blade operating conditions and health status, while the low generalization ability restricts the purely data-driven method based on machine learning;
(2) General vibration measurement methods can't be directly applied due to the severe working conditions (high rotating speed, high temperature, heavy load, etc.) of aero-engine blades, multi-source vibration coupling interference, and narrow space within the aero-engine (He et al. 2018), as a result, it is challenging to achieve the complete blade vibration information (frequency, amplitude, modal, etc.);
(3) There is no feasible theory and technology capable of the data fusion, interaction, and collaboration between the physical model and state information in physical space, thus, it is difficult to make full use of both model (prior) and measurement information (posterior) to realize real-time and accurate monitoring of blade crack damage.

In this context, the digital twin technology emerges (Grieves and Vickers 2017), making it possible to accurately quantify and identify the faults of a complex dynamic system, including aero-engine blade cracks. The SHM method based on digital twin simulates the behavior of the physical entity by building a "twin" in virtual space (Karve et al. 2020; Ritto and Rochinha 2021). To ensure the consistency between the physical entity and the digital entity, the model is updated with benchmark data to eliminate the error caused by the machining error, material defects, etc. Furthermore, with the real-time vibration data for rotating blade underlying performance degradation or under fault condition, the condition monitoring, fault diagnosis, and RUL prediction of blades can be conducted. Therefore, the application of digital twin needs not only the construction of accurate and efficient physical model but also the accurate measurement of operating condition for rotor blades in real-time. However, it is very hard in practical engineering to obtain accurate and complete information of blade vibration, which restricts the development of digital-twin-based blade crack detection and diagnosis. Therefore, this study decided to focus on the identification of blade vibration parameters, which is the key step for the construction of digital twin model.

Blade tip timing (BTT), as a non-contact stress measurement system (NSMS), measures the arrival time of blades by a few optical, capacitance, or magnetic sensors installed on the engine casing, and then obtains the blade vibration information based on some necessary BTT signal processing (also called reconstruction) method (Russhard 2010). Due to the non-contact property and the need for fewer probes for measurement, BTT technology attracts extensive attention from the aero-engine OEMs and academic fields. However, because of the severe under-sampling of BTT method itself, the vibration parameters and modes of blades cannot be directly obtained. As a result, many scholars are devoted to investigating the identification method of blade vibration parameters from the undersampled BTT signal. The earliest method relies on a strong prior assumption (Joung et al. 2006), where the blade vibration parameters can be identified with at least one sensor. For example (Guo et al. 2016) estimated the resonance frequency of the blade by utilizing arrival times between two probes without the once per revolution (OPR) signal. However, this is seriously inconsistent with the actual situation where the strong prior assumption is unavailable. Recently, many methods were proposed to conquer the limitation induced by the strong prior assumption (Chen et al. 2021). For example, the minimum variance spectral estimator (MVSE) was first used by (Stephan et al. 2008) to recover the complete frequency spectrum of BTT signals of mistuned bladed discs, and further improved by (Vercoutter et al. 2012). However, their methods still suffer some limitations, such as time-consuming and frequency aliasing. In order to further overcome the frequency aliasing, the methods of direction of arrival (DoA) estimation and compressed sensing are introduced into the spectrum analysis of BTT signal. (Lin et al. 2016) first tried to apply sparse representation to multi-mode blade vibration signals reconstruction. (Bouchain et al. 2019) considered the structured sparsity model to reduce the calculation time of signal reconstruction. With the physical constraints of probe arrangement, (Wu et al. 2019) proposed a sparse recovery algorithm for the vibration parameters of BTT signal based on the iterative reweighted L1-norm (IRL1). Liu et al. (2022) proposed an improved multiple signal classification (MUSIC) method to realize the displacement reconstruction of the undersampled signal. (Wang et al. 2022) further analyzed the influence of speed fluctuation on the theoretical arrival time and proposed a BTT method to achieve high-precision blade vibration measurement under rapid speed fluctuation conditions. The above-mentioned investigations are helpful for the in-depth understanding of the basic mechanism for the BTT-based blade vibration measurement and the reconstruction of the BTT undersampled signal. However, almost all the state-of-the-art identification methods for blade vibration parameters are on-the-grid methods, which may lead to frequency mismatch (also called base mismatch), and thus limit the accuracy of frequency

identification. Therefore, an effective off-the-grid method with acceptable computational time should be considered.

To overcome the basis mismatch (Chae et al. 2010) caused by gridding in compressed sensing methods, the atomic norm that constructs continuous dictionaries is introduced. (Candes and Fernandez-Granda 2014) first introduced a gridless sparse method for continuous-time signals by total variation norm. (Tang et al. 2013) proposed gridless compressed sensing, which can reconstruct spectrally sparse signals from random time-domain sampling by solving the atomic norm minimization problem, and further proposed the atomic norm soft thresholding (AST) method to promote the performance in the presence of noise. (Yang and Xie 2015) generalized AST to the case of incomplete data, and proposed an algorithm called GLS which satisfied incomplete data case. Other improvement methods include (Li and Chi 2016) for multi-measurement vector, (Wu et al. 2018) for low-rank matrix reconstruction, (Li et al. 2018) based on ANM for modal analysis, and (Wagner et al. 2021) for gridless DoA estimation. Actually, the BTT-based blade vibration measurement is the issue of multi-modal frequency reconstruction under the condition of extreme under-sampling, where the atomic norm-based continuous compressed sensing (CCS) that avodes the effect of basis mismatch facing with conventional methods can provide a novel insight to solve this problem from the perspective of super-resolution reconstruction.

In this paper, a gridless blade vibration parameter estimation method based on AST is proposed to avoid the reduction of frequency estimation accuracy caused by basis mismatch. The main contributions of this paper are illustrated as follows:

(1) A novel blade vibration reconstruction method based on atomic norm soft thresholding is proposed, where the atomic norm is harnessed to overcome the undersampling of BBT signals, and the gridless property is employed to conquer the base mismatch facing with the conventional sparse-based method.
(2) The proposed method not only improves the accuracy of frequency estimation but can also be performed by the proximal method in acceptable computational time.
(3) The comparative results of simulation and experiment show that the proposed method can effectively overcome the basis mismatch problem of most BTT algorithms. Meanwhile, the proposed method has stable performance and robustness with fewer data.

The remainder of the paper is organized as follows. Section 2 reviews the basic principle of BTT and basis mismatch. Section 3 describes the proposed method. Section 4 verifies the accuracy and robustness of the proposed method in the simulation case. Section 5 compares the performance of several methods by experiment data acquired from a test rig. Section 6 concludes the paper.

2 BTT reconstruction model and basis mismatch

In this section, the general principle of BTT is introduced first. With the conventional sparse reconstruction methods for BTT signal (Wu et al. 2019), the concept of basis mismatch, which is inevitable in on-the-grid methods, is explained theoretically. Given this, the off-the-grid compressed sensing based on the atomic norm is introduced to overcome the issue of basis mismatch.

2.1 Blade tip timing mechanism and reconstruction model

BTT obtains the vibration displacement of the blade tip by the time difference when the blade reaches the position of the BTT sensor in different states. Several non-contact probes are installed on the inner side of the aero-engine casing at a specific angle to measure the actual arrival time t_{act} of the blades. One of the probes is installed on the rotating shaft to obtain an OPR signal, which is used to measure the expected arrival time t_{exp} of the blades indirectly. And the displacement of circumferential vibration of the blade tip is given by:

$$x(t) = 2\pi R f_r(n)\left(t_{\exp} - t_{act}\right) \tag{1}$$

where R is the distance from the central axis of the rotor to the probe measuring point on the blade, $f_r(n)$ is the rotation frequency of the blade obtained at the nth revolution by OPR signal. The rotation speed between adjacent OPR pulses is generally considered to be constant. As Fig. 1 shows, assuming that q probes arranged circumferentially appear at Q predesigned positions at equal angles, the equivalent sampling rate of blade tip timing is $\frac{1}{2}Qf_r$ when rotation frequency is f_r. Therefore, the relationship between the fully sampled signal $\boldsymbol{y} \in \mathbb{R}^{NQ\times 1}$ and the undersampled signal of blade vibration $\boldsymbol{x} \in \mathbb{R}^{Nq\times 1}$ can be represented as follows:

$$\boldsymbol{x} = \boldsymbol{\Phi}\boldsymbol{y} \tag{2}$$

where $\boldsymbol{\Phi} = \begin{bmatrix} 1 & \cdots & \cdots & \cdots & \cdots & 0 \\ 0 & \cdots & 1 & \cdots & \cdots & 0 \\ \vdots & \vdots & \vdots & \vdots & \ddots & \vdots \\ 0 & \cdots & \cdots & 1 & \cdots & 0 \end{bmatrix} \in \mathbb{R}^{Nq\times NQ}$ is measurement matrix determined by the installation angle of probes. The number of rows of $\boldsymbol{\Phi}$ represents Nq points collected by N circles of q probes, and NQ represents the corresponding number of pre-designed positions, which means that the sampling frequency is equal to $\frac{1}{2}Qf_r$. Furthermore,

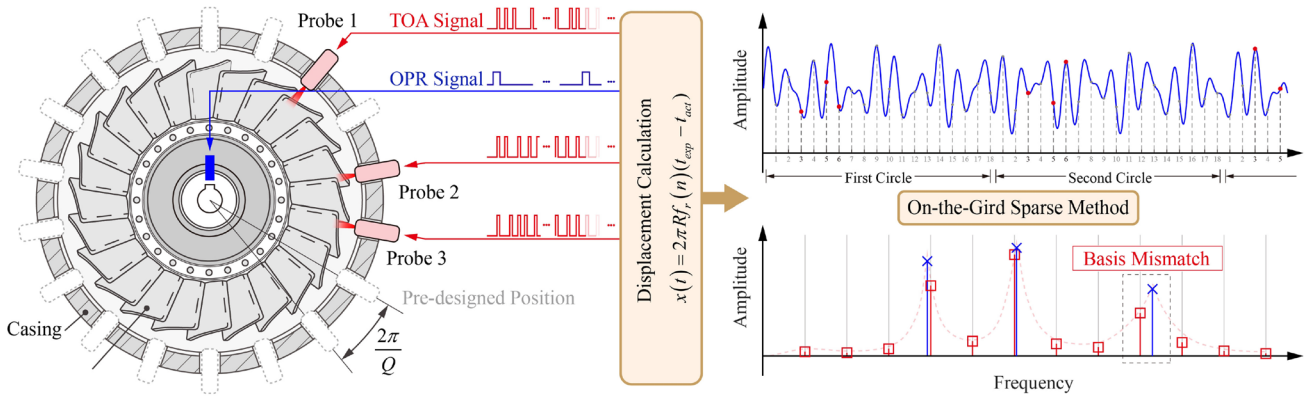

Fig. 1 BTT equivalent sampling model with $q = 3$ and $Q = 18$

considering the fact that the vibration response of the rotating blade tip is sparse in the frequency domain, Eq. (2) can be further expressed on the basis of sparse representation theory as follows,

$$\boldsymbol{x} = \boldsymbol{\Phi y} = \boldsymbol{\Phi\Psi\theta} \tag{3}$$

where $\boldsymbol{\Psi} = \left[\psi_1 \ \psi_2 \ \cdots \ \psi_m\right] \in \mathbb{R}^{NQ\times m}$ is transform matrix, also called sparse representation dictionary in conventional sparse-based methods, in this paper $\boldsymbol{\psi}$ refers to Fourier transform basis, $\boldsymbol{\theta} \in \mathbb{R}^{m\times 1}$ is the sparse representation coefficients.

According to Eq. (3), the compressed sensing theory can be applied to estimating multiple frequencies of the blade vibration signals undersampled by BTT. In other words, by selecting the appropriate sensing matrix, transform matrix, and sparse reconstruction algorithm, the original blade tip vibration displacement can be reconstructed with high probability and high accuracy. Moreover, the signal recovery is transformed into the identification of sparse representation coefficients $\boldsymbol{\theta}$. However, the strict equality constraint cannot be achieved considering the influence of noise and uncertainty. Given this, the equality constraint can be relaxed to the inequality constraint. Therefore, the obtained optimization problem is as follows:

$$\begin{aligned} &\hat{\boldsymbol{\theta}} = \arg\min_{\boldsymbol{\theta}\in\mathbb{R}^{m\times 1}} \|\boldsymbol{\theta}\|_0 \\ &\text{s.t.} \|\boldsymbol{x} - \boldsymbol{\Phi\Psi\theta}\|_2 \le \varepsilon \end{aligned} \tag{4}$$

Through orthogonal matching pursuit (OMP), L1-regularization, and other methods, the nonconvex optimization problem of Eq. (4) can be solved, thus realizing the estimation of blade vibration parameters.

2.2 Basis mismatch and the atomic norm

In 2.1, a critical assumption is given that the measured signal is sparse under the transform basis $\boldsymbol{\psi}$. Therefore, the signal needs to be discretized in the sparse representation domain (frequency domain). But, if the measured signal is recovered on the basis of $\boldsymbol{\Psi}_0$ instead of $\boldsymbol{\Psi}$, the error between the recovered signal and the measured signal may be increased. $\boldsymbol{\Psi}_1$ is defined as the closest subset of $\boldsymbol{\Psi}_0$ on $\boldsymbol{\Psi}$

$$\boldsymbol{\Psi_1} = \arg\min_{\psi\in\boldsymbol{\Psi}_0} \left\|\boldsymbol{\Psi}_0 - \boldsymbol{\Psi}\right\|_2 \tag{5}$$

Then, the compressively measured signal with basis mismatch is $\boldsymbol{x} = \boldsymbol{\Phi\Psi}_1\boldsymbol{\theta} + \boldsymbol{\Phi}\left(\boldsymbol{\Psi} - \boldsymbol{\Psi}_1\right)\boldsymbol{\theta}$. And, the measured signal recovery under $\boldsymbol{\Psi}_1$ is formulated as follows:

$$\begin{aligned} &\hat{\boldsymbol{\theta}}_1 = \arg\min_{\boldsymbol{\theta}\in\mathbb{R}^{m\times 1}} \|\boldsymbol{\theta}\|_1 \\ &\text{s.t.} \left\|\boldsymbol{x} - \boldsymbol{\Phi\Psi}_1\boldsymbol{\theta}\right\|_2 \le \varepsilon_{\text{bm}} \end{aligned} \tag{6}$$

where ε_{bm} is an upper bound on the basis mismatch error $\left\|\boldsymbol{\Phi}\left(\boldsymbol{\Psi} - \boldsymbol{\Psi}_1\right)\boldsymbol{\theta}\right\|_2$ (without noise). This error shows how good it is to approximate the assumed sparse vector $\hat{\boldsymbol{\theta}}_1$ of the Eq. (3) in the basis $\boldsymbol{\Psi}_1$, when actually $\hat{\boldsymbol{\theta}}_1$ is non-sparse or incompressible. In the case of basis mismatch, accurate signal recovery cannot be guaranteed and large errors may be suffered. As for the conventional sparse-based method, the error induced by basis mismatch can be reduced through proper grids. However, the error between actual frequencies (blue cross) and estimated frequencies (red square) will always exist(Chi et al. 2011), as shown in Fig. 1. Not only that, too fine grid division will increase the correlation between adjacent atoms, thus reducing the performance of the sparse recovery method.

To solve the basis mismatch, CCS or off-the-grid method is introduced. The CCS problem is solved by exploiting

sparsity, that is, the number of frequency components is as small as possible. Wherein, a direct sparse metric is the smallest number of frequency components composing $\boldsymbol{y}$, known as the atomic L0-norm, which can be denoted as:

$$\|\boldsymbol{y}\|_{\mathcal{A}} \triangleq \inf\left\{K : \boldsymbol{y} = \sum_{k=1}^{K} S_k \boldsymbol{a}_k\right\} \tag{7}$$

where $\boldsymbol{a}_k$ denotes a discrete sinusoid, and s_k is the corresponding coefficient. Similar to the L0-norm in the field of traditional compressed sensing, nonconvex and NP-hard make it difficult to solve the atomic L0-norm $\|\boldsymbol{y}\|_{A,0}$.Therefore, the atomic (L1) norm is introduced as a convex relaxation of the atomic L0-norm. It is assumed that the signal $\boldsymbol{y}$ can be represented as the non-negative combination of points from the atomic set A. The convex hull conv (A) of A is a compact set symmetrical with the origin center and contains the origin, as shown in Fig. 2. The atomic norm $\|\boldsymbol{y}\|_A$ defined by gauge function of conv (A) is denoted as:

$$\begin{aligned}\|\boldsymbol{y}\|_{\mathcal{A}} &\triangleq \inf\{t > 0 : \boldsymbol{y} \in t\mathrm{conv}(\mathcal{A})\} \\ &= \inf\left\{\sum\nolimits_k s_k : \boldsymbol{y} = \sum\nolimits_k s_k \boldsymbol{a}_k,\ s_k \geq 0,\ \boldsymbol{a}_k \in \mathcal{A}\right\}\end{aligned} \tag{8}$$

when $\boldsymbol{a}_k$ is the atomic set composed of 1-sparse elements, the atomic norm $\|\boldsymbol{y}\|_{\mathcal{A}}$ is the same as the L1-norm. Actually, the atomic norm can be generalized in sparse low-rank matrix, orthogonal matrix, and other fields. The main difference between CCS and traditional compressed sensing is that the observation dictionary is no longer composed of Fourier standard orthogonal basis that is discrete, but countless continuous atoms. And the correlation coefficient between atoms is close to 1. Because the dictionary set does not meet the Restricted Isometry Property (RIP), the traditional compressed sensing algorithm is no longer effective (Candes 2008). In contrast, the atomic norm $\|\boldsymbol{y}\|_A$ still has a good sparse constraint to the above continuous dictionary set.

It can be seen that the definition of the atomic norm is abstract and hard to be solved. According to the Caratheodory-Toeplitz theorem, the Vandermonde decomposition can be carried out for any positive semidefinite Toeplitz matrix. Based on this theorem, Proposition 2.1 in (Tang et al. 2013) provides proof of the relationship between the atomic norm and semidefinite programming (SDP). Thus, the atomic norm can be transformed into SDP:

$$\|\boldsymbol{y}\|_{\mathcal{A}} = \inf\left\{\frac{1}{2}(u_1 + t) : \begin{bmatrix}\mathrm{Toep}(\boldsymbol{u}) & \boldsymbol{y} \\ \boldsymbol{y}^* & t\end{bmatrix} \succeq 0\right\} \tag{9}$$

where $\boldsymbol{u} = \begin{bmatrix}u_1 & u_2 & \cdots & u_{NQ}\end{bmatrix} \in \mathbb{C}^{NQ}$, $(\cdot)^*$ denotes conjugate transpose and $\mathrm{Toep}(\boldsymbol{u}) \in \mathbb{C}^{NQ\times NQ}$ denotes the Hermitian Toeplitz matrix whose first column is equal to $\boldsymbol{u}$,

$$\mathrm{Toep}(\boldsymbol{u}) = \begin{bmatrix}u_1 & u_2 & \cdots & u_{NQ} \\ u_2^* & u_1 & \cdots & u_{NQ-1} \\ \vdots & \vdots & \ddots & \vdots \\ u_{NQ}^* & u_{NQ-1}^* & \cdots & u_1\end{bmatrix} \tag{10}$$

Equation (9) can be solved in polynomial time. Once the optimal solution $\hat{\boldsymbol{u}}$ is obtained, the frequency components encoded in Toep $(\boldsymbol{u})$ can be obtained by Vandermonde decomposition (Yang and Xie 2018).

3 AST for BTT signal

According to modal expansion theory, the fully sampled signal $\boldsymbol{y}$ of blade vibration can be written in the form of sinusoids as follows:

$$\boldsymbol{y} = \sum_{k=1}^{K} \boldsymbol{a}(f_k, \varphi_k) s_k = \begin{bmatrix}\boldsymbol{a}(f_1, \varphi_1) & \boldsymbol{a}(f_2, \varphi_2) & \cdots & \boldsymbol{a}(f_k, \varphi_k)\end{bmatrix}\boldsymbol{s} \tag{11}$$

where $\boldsymbol{a}(f_k, \varphi_k) = e^{j\varphi_k}\begin{bmatrix}0 & e^{j2\pi f_k} & \cdots & e^{j2\pi f_k(NQ-1)}\end{bmatrix}^{\mathrm{T}} \in \mathbb{C}^{NQ\times 1}$ is a vector with samples of individual sinusoids, $\boldsymbol{s} \in \mathbb{R}^{K\times 1}$ is the non-negative coefficients, $f_k \in [0, 1]$ and $\varphi_k \in [0, 2\pi]$ are the normalized frequency and the phase of the k^{th} component, respectively. And then, the atomic set $\mathcal{A}$ composed of $\boldsymbol{a}(f_k, \varphi_k)$ can be defined as:

$$\mathcal{A} = \{\boldsymbol{a}(f, \varphi) : f \in [0, 1],\ \varphi \in [0, 2\pi]\} \tag{12}$$

Therefore, the reconstruction of the fully sampled signal $\boldsymbol{y}$ from the BTT undersampled signal $\boldsymbol{x}$ can be expressed as the following optimization problem:

$$\begin{aligned}&\hat{\boldsymbol{y}} = \min_{\boldsymbol{y}} \|\boldsymbol{y}\|_{\mathcal{A}} \\ &\text{s.t.}\boldsymbol{x} = \boldsymbol{\Phi y}\end{aligned} \tag{13}$$

Considering the measurement noise in BTT signal, AST in (Bhaskar et al. 2013) inspired by the least absolute shrinkage and selection operator (LASSO) is introduced to recover the fully sampled signal $\boldsymbol{y}$ with additive Gaussian noise $e \sim N(0, \sigma^2)$:

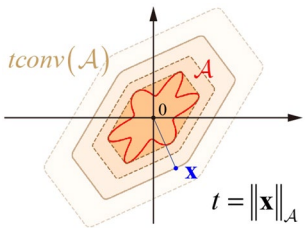

Fig. 2 The illustration of an atomic set $\mathcal{A}$ and its convex hull conv($\mathcal{A}$)

$$\hat{\boldsymbol{y}} = \arg\min_{\boldsymbol{y}} \frac{1}{2}\|\boldsymbol{x} - \boldsymbol{\Phi}\boldsymbol{y}\|_2^2 + \tau\|\boldsymbol{y}\|_{\mathcal{A}} \tag{14}$$

where τ is the regularization parameter. For the compressed sensing-based BTT signal reconstruction methods, the selection of regularization parameters is related to the balance between the data fidelity and the sparse prior. The optimal choice of the regularization parameter depends on the dual norm of noise which is mentioned in Theorem 1 of (Bhaskar et al. 2013). Accordingly, a good choice for τ is

$$\tau = \sigma\sqrt{\log(NQ) + \log(4\pi\log(NQ))} \tag{15}$$

Furthermore, Eq. (14) can be transformed into an SDP optimization problem.

$$\begin{aligned} &\min_{t,\boldsymbol{u},\boldsymbol{y}} \frac{1}{2}\|\boldsymbol{x} - \boldsymbol{\Phi}\boldsymbol{y}\|_2^2 + \frac{\tau}{2}(t + \mathrm{Tr}(\mathrm{Toep}(\boldsymbol{u}))) \\ &\text{s.t.}\tilde{\boldsymbol{S}} = \begin{bmatrix} \mathrm{Toep}(\boldsymbol{u}) & \boldsymbol{y} \\ \boldsymbol{y}^* & t \end{bmatrix},\ \tilde{\boldsymbol{S}} \succeq 0 \end{aligned} \tag{16}$$

SDP problem Eq. (16) can be solved by solvers such as SeDuMi, SDPT3 (Tutuncu et al. 2003), CVX (Wong and Zhou 2019), and CVXPY (Diamond and Boyd 2016). However, because SDP is a non-smooth convex optimization problem, the computational time of these solvers becomes unacceptable as the length of the signal increases ($NQ > 500$). Therefore, ADMM method that is proved to be an efficient solution algorithm for SDP problem (Bhaskar et al. 2013; Semper and Romer 2019) is introduced to better solve Eq. (16). Accordingly, one can obtain the augmented Lagrangian of Eq. (16), which is defined as

$$\begin{aligned} \mathcal{L}\left(t, \boldsymbol{u}, \boldsymbol{y}, \tilde{\boldsymbol{S}}, \boldsymbol{\Lambda}\right) = &\left\langle \boldsymbol{\Lambda}, \tilde{\boldsymbol{S}} - \begin{bmatrix} \mathrm{Toep}(\boldsymbol{u}) & \boldsymbol{y} \\ \boldsymbol{y}^* & t \end{bmatrix} \right\rangle + \frac{1}{2}\|\boldsymbol{x} - \boldsymbol{\Phi}\boldsymbol{y}\|_2^2 \\ &+ \frac{\tau}{2}(t + \mathrm{Tr}(\mathrm{Toep}(\boldsymbol{u}))) + \frac{\rho}{2}\left\|\tilde{\boldsymbol{S}} - \begin{bmatrix} \mathrm{Toep}(\boldsymbol{u}) & \boldsymbol{y} \\ \boldsymbol{y}^* & t \end{bmatrix}\right\|_F^2 \end{aligned} \tag{17}$$

where ρ is the penalty parameter, and $\boldsymbol{\Lambda}$ is the Lagrange multiplier variable which has the same partitioning of the blocks in $\begin{bmatrix} \mathrm{Toep}(\boldsymbol{u}) & \boldsymbol{y} \\ \boldsymbol{y}^* & t \end{bmatrix}$. Because ADMM optimizes each independent variable alternately when solving the function, the optimization step can be written as:

$$\left(t^{(i+1)}, \boldsymbol{u}^{(i+1)}, \boldsymbol{y}^{(i+1)}\right) \leftarrow \arg\min_{t,\boldsymbol{u},\boldsymbol{y}} \mathcal{L}\left(t, \boldsymbol{u}, \boldsymbol{y}, \tilde{\boldsymbol{S}}^{(i)}, \boldsymbol{\Lambda}^{(i)}\right) \tag{18}$$

$$\tilde{\boldsymbol{S}}^{(i+1)} \leftarrow \arg\min_{\tilde{\boldsymbol{S}} \succeq 0} \mathcal{L}\left(t^{(i+1)}, \boldsymbol{u}^{(i+1)}, \boldsymbol{y}^{(i+1)}, \tilde{\boldsymbol{S}}, \boldsymbol{\Lambda}^{(i)}\right) \tag{19}$$

$$\boldsymbol{\Lambda}^{(i+1)} \leftarrow \boldsymbol{\Lambda}^{(i+1)} + \rho\left(\tilde{\boldsymbol{S}}^{(i+1)} - \begin{bmatrix} \mathrm{Toep}\left(\boldsymbol{u}^{(i+1)}\right) & \boldsymbol{y}^{(i+1)} \\ \boldsymbol{y}^{*(i+1)} & t^{(i+1)} \end{bmatrix}\right) \tag{20}$$

wherein, in Eq. (18), the corresponding closed-form solution can be obtained by taking the derivatives of the matrix and setting the derivative equal to 0. And then, the updates step is given as follows:

$$t^{(i+1)} = \frac{1}{\rho}\Lambda_t^{(i)} + \boldsymbol{S}_t^{(i)} - \boldsymbol{I}\frac{\tau}{2\rho} \tag{21}$$

$$\boldsymbol{u}^{(i+1)} = \frac{1}{\mathfrak{D}(\mathbf{1})}\left(\mathfrak{D}\left(\tilde{\boldsymbol{S}}_{\boldsymbol{u}}^{(i)} + \frac{1}{\rho}\boldsymbol{\Lambda}_{\boldsymbol{u}}^{(i)}\right) - \frac{\tau}{2\rho}\boldsymbol{i}_1\right) \tag{22}$$

$$\boldsymbol{y}^{(i+1)} = \left(\frac{1}{2}\boldsymbol{\Phi}^*\boldsymbol{\Phi} + \rho\boldsymbol{I}\right)^{-1}\left(\rho\tilde{\boldsymbol{S}}_{\boldsymbol{y}}^{(i)} + \boldsymbol{\Lambda}_{\boldsymbol{y}}^{(i)} + \frac{1}{2}\boldsymbol{\Phi}^*\boldsymbol{x}\right) \tag{23}$$

where $\mathbf{1}$ is a matrix with all entries equal to 1, $\boldsymbol{i}_1$ is a vector, in which only the first entry is equal to 1, and the rest are all equal to 0, $\mathfrak{D}(\cdot)$ is an operator that returns a vector with the same dimensions as $\boldsymbol{u}$, and the ith entry in $\mathfrak{D}(\cdot)$ is the sum of the ith diagonal line of the input matrix. Afterwards, the updates step of $\tilde{\boldsymbol{S}}$ is the orthogonal projection on SDP cone,

$$\tilde{\boldsymbol{S}}^{(i+1)} = \mathrm{P}_{\mathrm{SDP}}\left(\tilde{\boldsymbol{S}}^{(i)} - \begin{bmatrix} \mathrm{Toep}\left(\boldsymbol{u}^{(i+1)}\right) & \boldsymbol{y}^{(i+1)} \\ \boldsymbol{y}^{*(i+1)} & t^{(i+1)} \end{bmatrix} + \frac{1}{\rho}\boldsymbol{\Lambda}^{(i)}\right) \tag{24}$$

With Eqs. (20)–(24), one iteration of ADMM can be carried out, and algorithm 1 is the example that describes the specific step of ADMM.

Algorithm 1: The ADMM algorithm for solving the SDP problem

Input: observed signal under-sampling $\boldsymbol{x}$, sensing matrix $\boldsymbol{\Phi}$, regularization parameter τ, penalty parameter ρ
Output: recovered signal fully-sampling $\boldsymbol{y}$
Begin
Calculate $\left(\frac{1}{2}\boldsymbol{\Phi}^*\boldsymbol{\Phi} + \rho\boldsymbol{I}\right)^{-1}$
Initialize $\tilde{\boldsymbol{S}}^{(0)}$, $\boldsymbol{\Lambda}^{(0)}$
  for $i = 0, \ldots, N_{\max\_\mathrm{ite}}$ **do**
    update $\boldsymbol{y}^{(i+1)}$, $\boldsymbol{u}^{(i+1)}$, $t^{(i+1)}$, $\tilde{\boldsymbol{S}}^{(i+1)}$, $\boldsymbol{\Lambda}^{(i+1)}$
    $i \leftarrow i + 1$
    if stopping criteria are satisfied **do**
      Stop iteration
    end if
end for
Return $\boldsymbol{y}^{(i+1)}$,$\boldsymbol{u}^{(i+1)}$

By solving the SDP problem, the optimal solution of the signal $\hat{\boldsymbol{y}}$ and the Toeplitz matrix $\mathrm{Toep}(\boldsymbol{u})$ can be obtained. However, if the frequency of the fully sampled signal is estimated directly by Fourier transform of $\hat{\boldsymbol{y}}$, the gridless advantage brought by the atomic norm will be lost. Therefore, the dual norm of the atomic norm, Vandermonde decomposition (Yang and Xie 2018; Li et al. 2020), and other methods are used to locate the frequency. In this study, the dual norm of the atomic norm is employed, which can be defined as:

$$\begin{aligned}\|z\|_{\mathcal{A}}^{*} &= \sup_{\boldsymbol{a}\in\mathcal{A}} \langle z, \boldsymbol{a}(f,\varphi)\rangle_{\mathbb{R}} \\ &= \sup_{f\in[0,1],\varphi\in[0,2\pi]} \left\langle z, e^{i\varphi}\boldsymbol{a}(f,0)\right\rangle_{\mathbb{R}} \\ &= \sup_{f\in[0,1]} \left|\sum_i z_i e^{-j2\pi fi}\right|\end{aligned} \tag{25}$$

where $\langle\cdot\rangle_{\mathbb{R}}$ denotes real inner product. The form of dual norm is equivalent to the maximum modulus of polynomial $Q(f)=\sum_i z_i e^{-j2\pi fi}$, $f\in[0,1]$ in the unit circle. Thus, the dual problem of Eq. (14) is defined as:

$$\begin{aligned}&\max_{z} \frac{1}{2}\|y\|_2^2 - \frac{1}{2}\|\boldsymbol{\Phi y} - z\|_2^2 \\ &\text{s.t.}\|z\|_{\mathcal{A}}^{*} \le \tau\end{aligned} \tag{26}$$

According to Slater's condition, there is a strong duality between the original problem and the dual problem. Theorem 2.4 in (Tang et al. 2013) guarantees the uniqueness of the optimal solution.

Corollary 1 *Suppose for* $\boldsymbol{a}(f,0)$ *in the atomic set* $\boldsymbol{a}(\boldsymbol{f},0)\in\mathcal{A}$, *and* $\hat{\boldsymbol{z}}$ *is the optimal solution of Eq.* (26) *satisfying*.

$$\langle \hat{z}, \hat{\boldsymbol{y}}\rangle_{\mathbb{R}} = \tau\|\boldsymbol{y}\|_{\mathcal{A}} \tag{27}$$

$$\left|\left\langle \hat{z}, \boldsymbol{a}(f_i,0)\right\rangle\right| = \tau,\ \forall f_i \in \boldsymbol{f} \tag{28}$$

$$\left|\left\langle \hat{z}, \boldsymbol{a}(f_i,0)\right\rangle\right| < \tau,\ \forall f_i \notin \boldsymbol{f} \tag{29}$$

Once the recovery signal $\hat{\boldsymbol{y}}$ in Eq. (11) is solved, the solution $\hat{\boldsymbol{z}} = \boldsymbol{\Phi}^{*}(\boldsymbol{x} - \boldsymbol{\Phi}\hat{\boldsymbol{y}})$ of dual problem Eq. (26) can be obtained. Eq. (28) and Eq. (29) show unique properties that can localize frequencies. The modulus of dual polynomial $Q(f_i) = \left\langle \hat{z}, \boldsymbol{a}(f_i,0)\right\rangle$ ($\hat{z}$ for Fast Fourier transform) reaches the maximum when frequencies belong to the support set $\hat{\boldsymbol{f}} = [\hat{f}_1\ \hat{f}_2\ \cdots\ \hat{f}_K\ ]$. The estimation accuracy of frequency can be improved with the number of Fast Fourier points, so fine grids can be divided to obtain excellent frequency resolution. In the presence of noise, under-sampling and speed fluctuation, some aliasing frequencies in the red region shown in Fig. 3a may appear. Therefore, low-precision frequency estimation can be achieved by recovery signal $\hat{\boldsymbol{y}}$ at first, and then high-precision frequency estimation can be performed by the dual norm. After that, the least square method could calculate the amplitude after the accurate frequency support set $\hat{\boldsymbol{f}}$ is obtained.

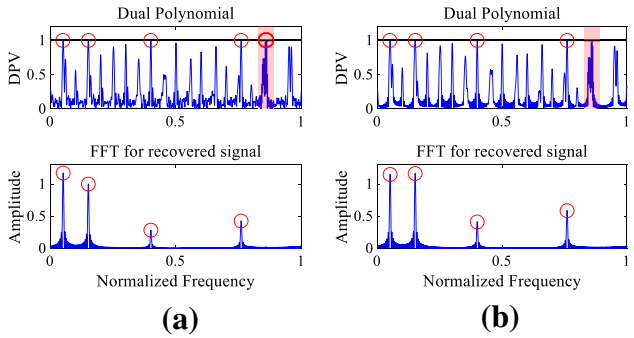

Fig. 3 Dual polynomial value (DPV, the maximum value is normalized to 1) and FFT spectrum for recovered signal, **a** SNR = 20 dB and **b** without noise

4 Numerical verification

In this section, the validity of the proposed method for the reconstruction of BTT undersampled signal is numerically verified. According to BTT equivalent sampling model, the synthetic signal is used for verification and comparison with other reconstruction methods. Moreover, the BTT simulator that is always used in BTT algorithm verification is employed to evaluate the performance in signal reconstruction.

4.1 Synthetic signal-based verification

The synthetic signal with under-sampling and non-uniformity is constructed to verify the validity of the proposed method. In recent years, many scholars have been devoted to this field, pursuing an effective way to overcome the undersampling and non-uniformity of BTT signals. Several methods such as MVSE(Stephan et al. 2008), OMP(Bouchain et al. 2019), and MUSIC(Wang et al. 2020) have been widely used in BTT signal processing. MVSE was put forward by Capon, and it was applied in BTT very early. OMP is a greedy algorithm for solving signal recovery. MUSIC and MVSE belong to direction of arrival (DoA) algorithms, and the improved MUSIC is effective in BTT data processing.

To preliminarily verify the performance of the proposed method, the synthetic signal is used to compare the proposed method with several existing methods. The frequencies of the synthetic signal are normalized by the equivalent sampling frequency $\frac{1}{2}Qf_r$. Four frequency components $f_1=0.2353, f_2=0.3055, f_3=0.6011$ and $f_4=0.8256$ with amplitude $c_1=0.5$, $c_2=1.2$, $c_3=1.7$ and $c_4=0.4$, respectively. At the same time, white Gaussian noise with $SNR=15$ dB is added to the synthetic signal. The minimum installation interval of the probe is 36°, which means ten pre-designed positions with equal circumferential angles are

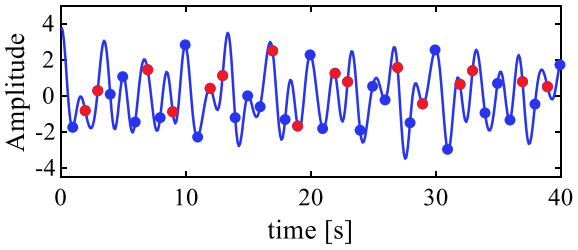

Fig. 4 The real part of the synthetic signal without noise in the first case

given, and three different probes arrangement cases are considered. In the first case, the number of probes is four, and the index is $[2\ 3\ 7\ 9]$. The index of probes in the second and third cases is $[2\ 3\ 7]$ and $[2\ 3]$, respectively. The signal observed in the first case is illustrated in Fig. 4. The red dot indicates the observed value from probes, and the blue dot indicates the unknown value in the pre-designed position. In all three cases, 20 circles of data were selected.

The signal spectrum obtained by different methods is shown in Figs. 5, 6, 7, 8. Before comparing the differences among the results, it should be noted that OMP, MVSE, and

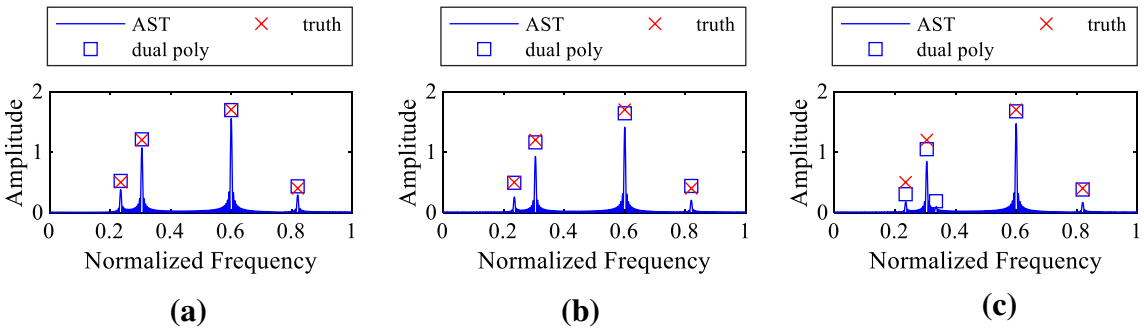

Fig. 5 The spectrum of synthetic signals obtained by AST in three cases, **a** $q=4$, **b** $q=3$, and **c** $q=2$

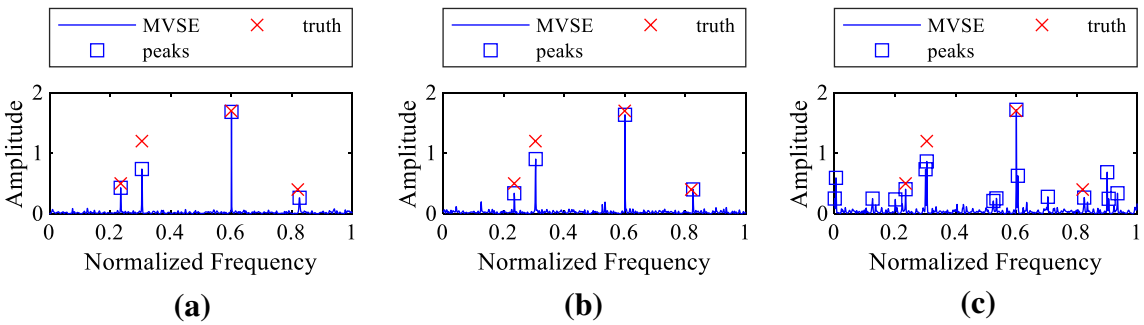

Fig. 6 The spectrum of synthetic signal obtained by MVSE in three cases, **a** $q=4$, **b** $q=3$, and **c** $q=2$

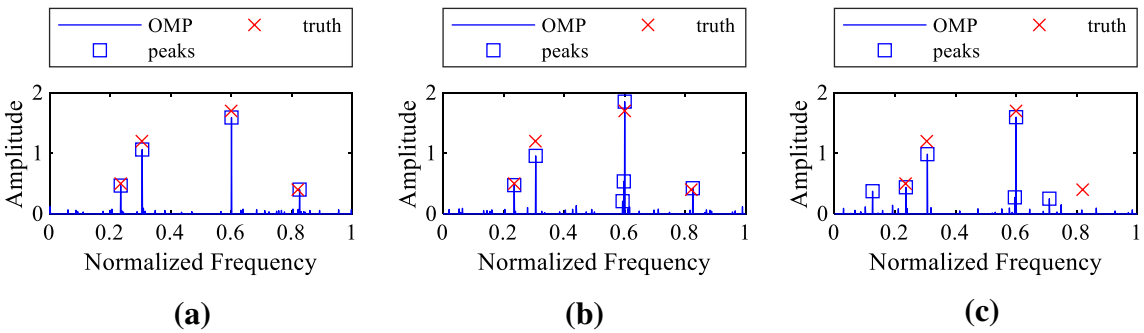

Fig. 7 The spectrum of synthetic signal obtained by OMP in three cases, **a** $q=4$, **b** $q=3$, and **c** $q=2$

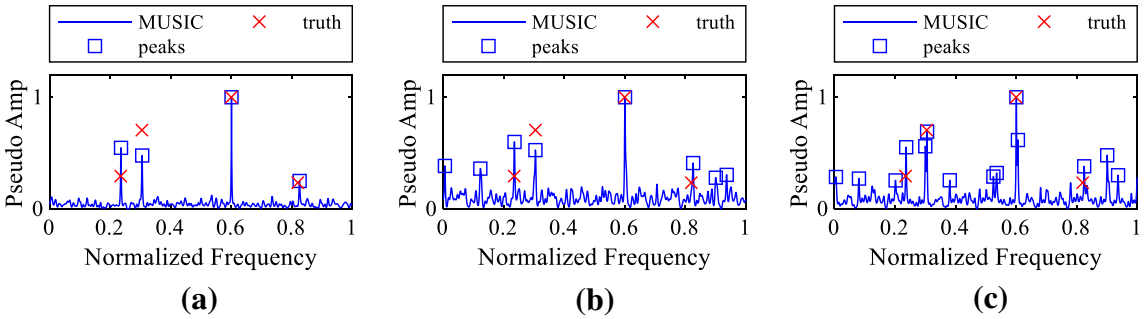

Fig. 8 The spectrum of synthetic signal obtained by MUSIC in three cases, **a** $q=4$, **b** $q=3$, and **c** $q=2$

Table 1 Frequency and amplitude RMSE of the estimation result under three cases

Methods	$q=4$		$q=3$		$q=2$	
	Frequency	Amplitude	Frequency	Amplitude	Frequency	Amplitude
AST	**0.0000933**	**0.01051**	**0.0001058**	**0.02071**	**0.0000916**	**0.06271**
MVSE	0.0001785	0.12154	0.0001785	0.08591	0.0002106	0.09326
OMP	0.0001785	0.04473	0.0003455	0.07210	–	–
MUSIC	0.0002385	–	0.0002385	–	0.0004684	–

The Bold font indicates the best result under the same entry

MUSIC are all on-the-grid methods. To reflect the effects of basis mismatch for these on-the-grid methods, the grid size of these three methods is selected as 0.001. The spectrum in Fig. 5 is obtained by a fast Fourier transform of the reconstructed fully sampled signal $\hat{\boldsymbol{y}}$. However, in order to obtain a more accurate frequency estimation, the frequency and amplitude (blue square in Fig. 5) is estimated using the property of dual polynomials. OMP and MVSE can estimate the amplitude of the signal, so these peaks in the spectrum are directly used to represent the information in the original signal. The pseudo spectrum obtained by MUSIC method could not indicate the amplitude value, so the result of MUSIC is normalized to [0, 1], and only the frequency estimation accuracy will be compared with others. Table. 1 shows the frequency and amplitude root mean square error (RMSE) of the estimation results, and the null value in the table indicates that the frequency or amplitude of the signal cannot be estimated under the corresponding cases.

In the first case, all four methods can get good frequency estimation results, as shown in Figs. 5a, 6, 7, 8a. And Table 1 shows that AST with dual polynomial has the highest estimation accuracy. Due to the small number of points, the amplitude estimation accuracy of OMP and MVSE is lower than AST, which can be improved by increasing the signal length. When q is reduced to 3, the estimation result of MUSIC is greatly affected. It can be seen from Fig. 8b that the frequency components with smaller amplitude are not easily distinguished for the appearance of aliasing frequency and the influence of noise. The other three methods maintain good frequency estimation accuracy, but the amplitude estimation accuracy drops. In the third case, the number of probes becomes 2 (minimum number), and only AST gets acceptable results, as Fig. 5c shows. AST can achieve the best estimation results under different probe numbers.

Table 2 The RMSE and R-square of the reconstructed signal obtained by AST, MVSE, and OMP

Methods	With basis mismatch		Without basis mismatch	
	RMSE	R-square	RMSE	R-square
AST	**0.164**	**0.994**	**0.072**	**0.998**
MVSE	0.425	0.960	0.227	0.988
OMP	0.685	0.895	0.435	0.958

The Bold font indicates the best result under the same entry

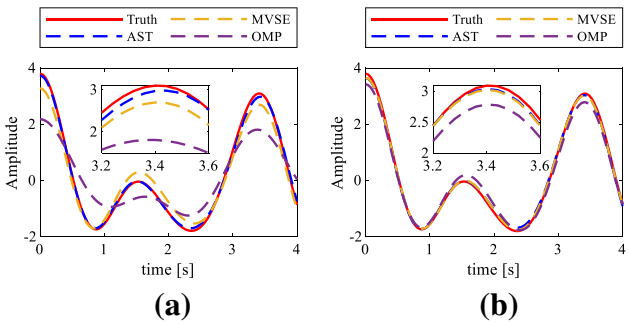

Fig. 9 The reconstructed signals obtained by AST, MVSE, and OMP under $q=3$, **a** With basis mismatch and **b** Without basis mismatch

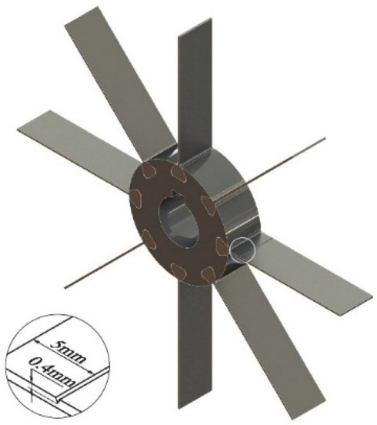

Fig. 10 The modal of the blade disk with crack

To better illustrate the influence of basis mismatch on these methods, the second case, where q is equal to 3, is further analyzed. The results affected by basis mismatch are shown in Figs. 5b, 6, 7, 8b. To avoid basis mismatch, the frequency resolution of the synthetic signal is approximated to three decimal places, which is consistent with the grid size 0.001. The synthetic signal is reconstructed by using the spectrum obtained by MVSE, OMP, and the proposed AST. It should be noted that the results obtained by MUSIC are not involved in this case because of the lack of amplitude. The RMSE and R-square of the reconstructed signal obtained by AST, MVSE, and OMP are shown in Table 2, and, correspondingly, the reconstructed signals are shown in Fig. 9. Since the estimated frequency and amplitude are both affected by basis mismatch, it can be seen from Fig. 9 that the reconstruction error of the signals obtained by MVSE and OMP is much smaller when there is no influence of basis mismatch. Wherein, OMP suffers the most apparent performance degradation, which is attributed to the misalignment of the actual sparsity basis with DFT basis (Chi et al. 2011). For AST, there is no increase in signal reconstruction error caused by basis mismatch, and even without basis mismatch. It can be noted from Table 2 that the proposed AST has the lowest signal reconstruction error.

4.2 BTT simulator-based verification

The effectiveness of the proposed method is further verified by the BTT simulator that is extensively used for BTT signal reconstruction methods evaluation (Mohamed et al. 2020; Wei et al. 2022). In this study, the dynamic model used for BTT simulator is composed of three parts: blade unit, rotor unit, and disk unit, as shown in Fig. 10. Beam element is used to construct the basic dynamic differential equations of the BTT simulator, where the elastic deformation of the disk is ignored, and the bearing is considered as a linear spring damping model. Then, the dynamic model of the rotor blade coupling system can be obtained as follows:

$$\boldsymbol{M}\ddot{\boldsymbol{q}} + (\boldsymbol{C} + \boldsymbol{G})\dot{\boldsymbol{q}} + \boldsymbol{K}\boldsymbol{q} = \boldsymbol{F}(t) \tag{30}$$

where $\boldsymbol{q}$ is the displacement response vector of the system, $\boldsymbol{F}$ is the centrifugal force vector concerning the time, $\boldsymbol{M}$, $\boldsymbol{C}$, $\boldsymbol{G}$ and $\boldsymbol{K}$ represent mass matrix, structural damping matrix, Coriolis matrix, and static stiffness matrix. Since the formulation of the dynamic model is beyond the scope of this study, it will not be presented in this paper. For more details, please refer to our previous study (Yang et al. 2021a, c; Yang et al. 2022) and the open-access literature (Li et al. 2019).

The material and geometrical parameters of the blade disk are shown in the Table 3. In this study, it is assumed that a crack is parallel to the blade width direction in a blade,

Table 3 Material and geometrical parameters

Material parameters	Value	Geometrical parameters	Value
Yang's module of disk	2.09×10^{11} N m^{-2}	Thickness of disk	2.0×10^{-2} m
Density of disk	7.85×10^{3} kg m^{-3}	Radius of disk	5.0×10^{-2} m
Yang's module of blade	7×10^{10} N m^{-2}	Length of blade	4.8×10^{-2} m
Density of blade	2.71×10^{3} kg m^{-3}	Thickness of blade	1.0×10^{-3} m
Poisson's ratio of blade	0.33	Number of blades	8

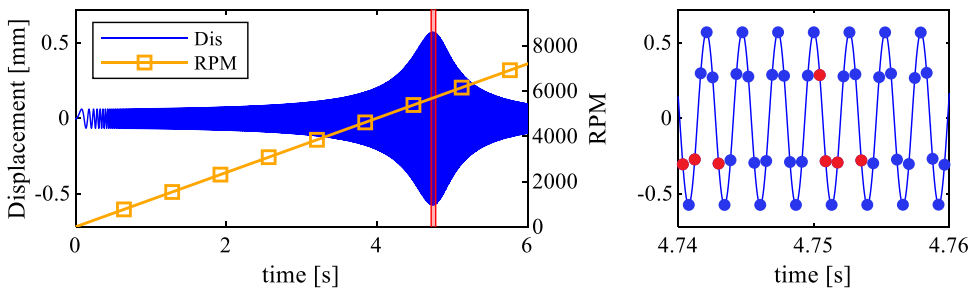

Fig. 11 Displacement response of norm blade and resonance occurs at 5700RPM

as shown in Fig. 10. The distance between the crack and the blade root is 5×10^{-3} m, and the depth of the crack is 4×10^{-4} m. The harmonic excitation is applied to the blade. Then the displacement response of BTT measuring point (middle point of blade tip) is calculated by Newmark-β method. When the rotation speed rises from 0 to 7200 RPM with an acceleration of 20 Hz/s, the displacement responses at BTT measuring points of normal blade and blade with crack are shown in Figs. 11 and 12. The enlarged view of the red area is on the right side of Figs. 11 and 12. Twenty-four equally spaced probes pre-designed positions (blue points) are given, and index of probes is $\begin{bmatrix}0 & 1 & 3 & 7\end{bmatrix}$. In addition, the simulated BTT signal is sampled in a form (red points in Figs. 11 and 12) according to BTT probe arrangement.

Because the measurement point of the probe is designed in the middle of the blade tip, the modes above the second order are very weak in the experiment. Therefore, only the first mode is considered in this simulation. The first-order resonance of the normal blade occurs at about 5700 RPM. The resonance frequency is 379.41 Hz after the FFT of all sampled signals in the resonance region. The resonance region of the crack blade appears at about 5460 RPM, and the corresponding resonance frequency is 363.38 Hz after FFT. Selecting the data corresponding to the resonance area and sampling according to the arrangement mode of BTT probes, dual polynomials, and frequency support set obtained by AST is shown in Fig. 13. Crack causes integral multiples of the fundamental frequency, but these frequency components are very weak which usually two orders of magnitude different from the amplitude of the fundamental frequency. It can be seen in Table 4 that the first-order natural frequency of the cracked blade drops. However, the $\times2$ and $\times3$ frequency are too weak to be reflected in the dual polynomial. According to the above two results, it can be seen that frequency has a much higher estimation accuracy than amplitude. At the same time, the appearance of cracks will also lead to an increase in amplitude estimation error and signal reconstruction error.

5 Experimental verification

5.1 Test rig with BTT system

The data from the real test rig is used to compare the proposed method with other methods. The bladed disk with

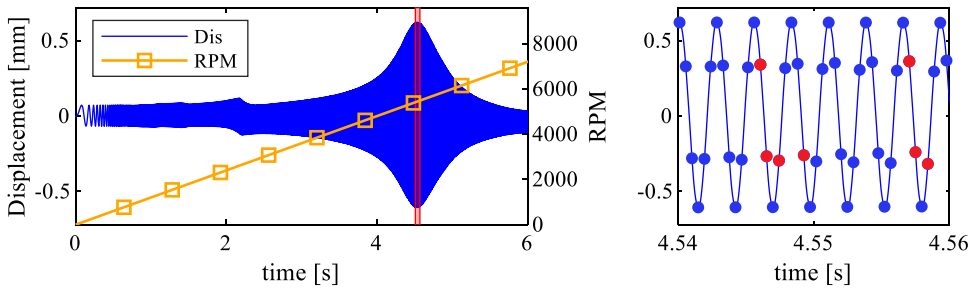

Fig. 12 Displacement response of crack blade and resonance occurs at 5460RPM

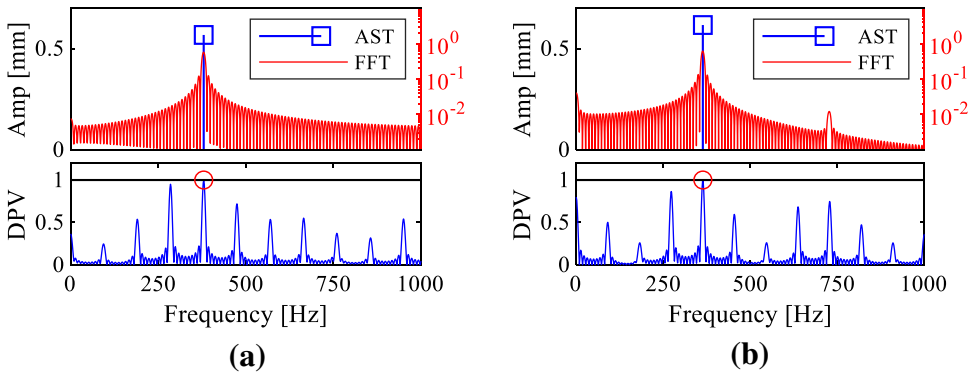

Fig. 13 The spectrum and dual polynomial value (the maximum value is normalized to 1) of simulated signal **a** normal blade and **b** crack blade

Table 4 Estimation result of AST

Signals	Frequency		Amplitude		R-square
	AST	Truth	AST	Truth	
Normal blade	379.69 Hz	379.41 Hz	0.5673 mm	0.5675 mm	0.996
Crack blade	363.73 Hz	363.38 Hz	0.6163 mm	0.6100 mm	0.993

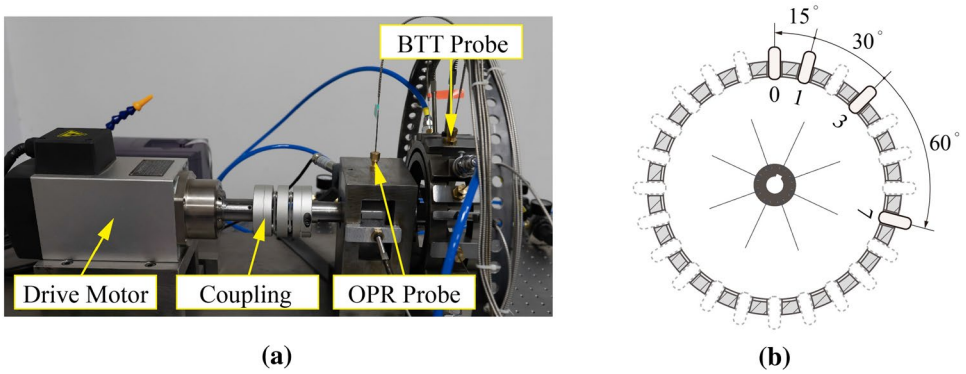

Fig. 14 The test rig with BTT system. **a** the test rig and **b** the arrangement of BTT probes

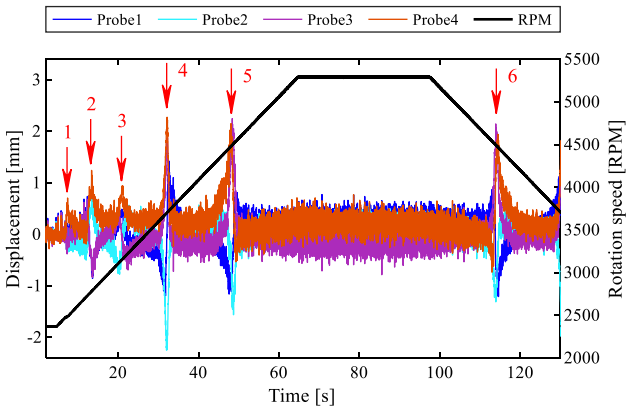

Fig. 15 The displacement measured by 4 BTT probes for blade 1

the same physical parameters and material as the bladed disk shown in Fig. 10 is selected as the test part. Two air nozzles placed at 180° are used to generate air excitation. As shown in Fig. 14a, the blade disk in test rig is driven by a motor from 2300 to 5300 RPM. The rotation speed of the test rig decreased after 30 s at 5300 RPM. Four BTT probes are installed around with the installation angle $[0°\ 15°\ 30°\ 60°]$, which is equivalent to the installation with index $[0\ 1\ 3\ 7]$ in 24 pre-designed positions in Fig. 14. The pulse from BTT probes is collected by EMTD system. And Blade 1 is taken as an example. The displacement of the blade tip is shown in Fig. 15. The red arrow in Fig. 15 indicates several resonance regions of the blade.

5.2 Frequency estimation

In this section, MUSIC, OMP, and MVSE mentioned in 4.1 are used to compare with AST, and fewer data points will be intercepted. Ten circles of data at the 40 s in Fig. 15, and the corresponding rotating speed is 4080 RPM. According to the theoretical vibration analysis, the first-order natural frequency of the blade under this rotating speed is 367.88 Hz. The regularization parameter in AST is obtained by Eq. (15). The width of snapshots matrix in MUSIC is set to 32. The sparsity of OMP is set to 10. And the iteration number of autocorrelation matrix in MVSE is set to 10.

The signal spectrum obtained by four methods, i.e., MUSIC, OMP, MVSE, and AST, is shown in Fig. 16. The solid blue line in these figures represents the rotating speeds of the bladed disk and its integer multiple. The red dotted line indicates the natural frequency. First, only the result of AST can intuitively find the natural frequency. The pseudo spectrum of the signal obtained by MUSIC can discover the weak natural frequency in Fig. 15a, d, and e. MVSE and OMP are challenging to locate the natural frequency, and only some integer multiples of the revolution frequency can be distinguished.

As no contact measurement method such as strain gauge is installed on this test rig, MUSIC, which has been widely verified, is used as a reference. But 100 circle data at the same speed are selected to ensure accurate results. Table 5 shows the natural frequencies obtained from AST and MUSIC. It can be seen that the natural frequencies of different blades vary widely, and the difference between blade 2 with the largest natural frequency (376.69 Hz) and blade 3 with the lowest natural frequency (365.20 Hz) is 11.49 Hz. This is caused by machining errors which are also called the mistuning of the blade. AST can maintain good frequency estimation accuracy with fewer sampling points and has a stable performance like MUSIC in the non-resonant region. These points show that the proposed method has a strong sparse constraint brought by the atomic norm and good noise robustness from soft threshold noise reduction.

6 Conclusions

This paper presents an AST-based blade vibration reconstruction method, where the off-the-grid CCS is introduced to solve the basis mismatch and overcome the under-sampling problem. The proposed method may serve as the enabling technology for digital twin-based blade health monitoring offering high-precision blade vibration parameters. Both numerical simulation and experimental verification are

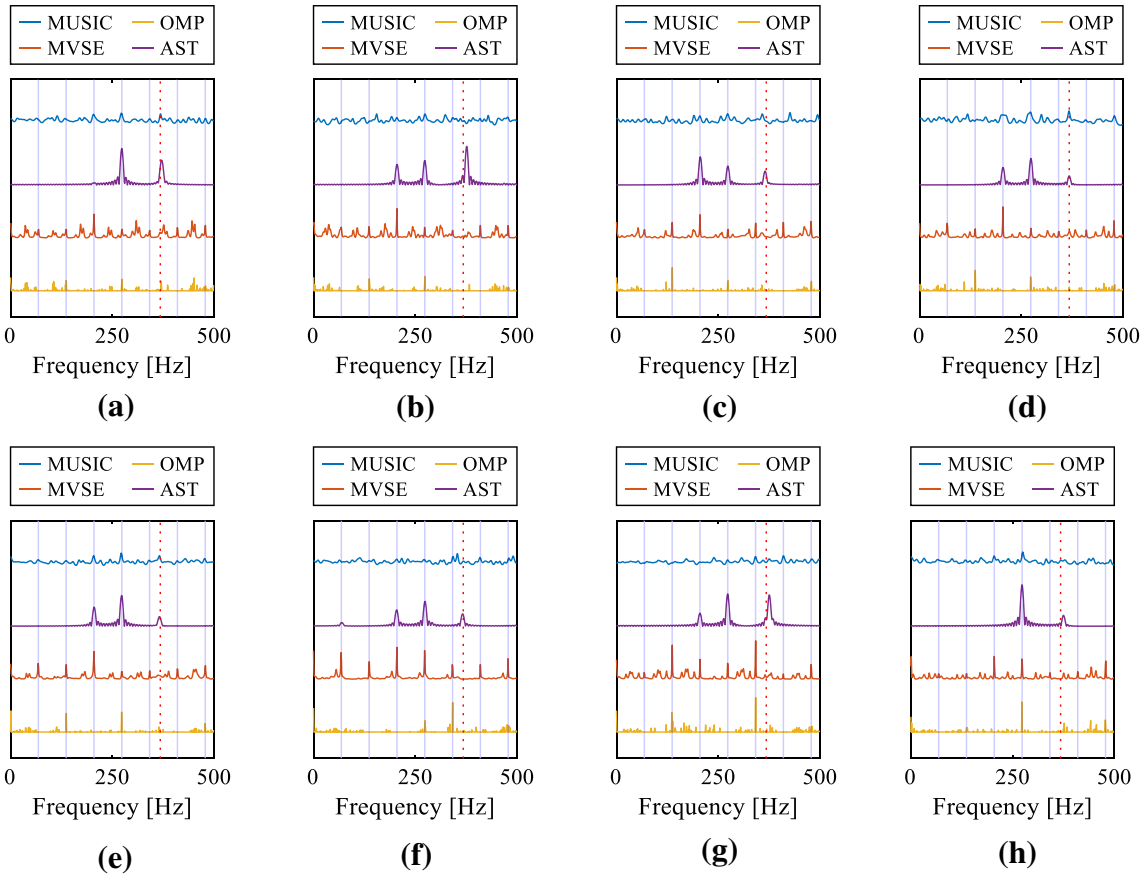

Fig. 16 The spectrum of 8 blades obtained by MUSIC, AST, MVSE, and AST. **a** Blade 1, **b** Blade 2, **c** Blade 3, **d** Blade 4, **e** Blade 5, **f** Blade 6, **g** Blade 7, **h** Blade 8

Table 5 First-order natural frequencies of eight blades obtained by AST and MUSIC

No	Nature frequency		No	Nature frequency	
	AST	Truth obtained by MUSIC		AST	Truth obtained by MUSIC
Blade 1	371.77 Hz	371.83 Hz	Blade 2	376.69 Hz	377.15 Hz
Blade 3	365.20 Hz	365.31 Hz	Blade 4	367.67 Hz	367.54 Hz
Blade 5	366.02 Hz	367.12 Hz	Blade 6	366.85 Hz	366.67 Hz
Blade 7	375.87 Hz	375.72 Hz	Blade 8	375.05 Hz	374.16 Hz

performed to verify the validity of the proposed method. The following conclusions can be drawn as follows:

(1) The general problem of BTT signal reconstruction is obtained through the equivalent sampling model of BTT. The atomic norm is used instead of L1-norm in the traditional method. Thus, approximating infinite frequency identification accuracy could be achieved. To solve the optimization problem containing the atomic norm, the primal problem is converted into SDP, and ADMM is used to solve it efficiently. Finally, the excellent property of dual norm of the atomic norm is used to obtain an accurate frequency support set.

(2) In the simulation part, the data from synthetic signal showed that the proposed method has better performance in the frequency and amplitude estimation, especially with fewer probes. After that, the data generated by the blade disk dynamic model are used to preliminarily verify that the proposed method can accurately extract the natural frequency and other information when the data is incomplete. Experiments data further demonstrate that the proposed method can effectively overcome the negative factors, including non-uniformity, under-sampling, fewer data, and noise in actual measurement.

This study preliminarily proves that the method based on the atomic norm performs quite well in reconstructing BTT signal. However, there is still a gap to be improved. ADMM-based AST can be solved with low time-consuming, but large memory occupation and high complexity limit the

proposed method applied on a large scale. In addition, a regularization parameter selection method suitable for BTT data should be proposed to improve computational efficiency. And the sensing matrix should be reorganized to satisfy the various probes' layout. Moreover, a high-efficiency algorithm and strict proof for semidefinite relaxation will be promoted in the future.

Acknowledgements We thank the support given by the National Natural Science Foundation of China (52105117 & 51875433), the National Key Research and Development Program of China (2020YFB2010800), and the Funds for Distinguished Young talent of Shaanxi Province (No. 2019JC-04).

Author contributions Ruo Chen Jin: orignal draft, method implementation, experimental validation Laihao Yang: supervisor, funding, method Zhibo Yang (phdapple@mail.xjtu.edu.cn): co-supervisor, funding, method Yu Sun: method, discussion Ruqiang Yan: funding, discussion Xuefeng Chen: discussion.

Declarations

Conflict of interest The authors declare that they have no conflict of interest.

Replication of results Experimental data and the Python based source code for replication of the case studies will be available from the corresponding author upon request.

References

Abbas M, Shafiee M (2018) Structural health monitoring (SHM) and determination of surface defects in large metallic structures using ultrasonic guided waves. Sensors-Basel 18(11):3958

Bhaskar BN, Tang GG, Recht B (2013) Atomic norm denoising with applications to line spectral estimation. IEEE T Signal Proces 61(23):5987–5999

Bouchain A, Picheral J, Lahalle E, Chardon G, Vercoutter A, Talon A (2019) Blade vibration study by spectral analysis of tip-timing signals with OMP algorithm. Mech Syst Signal Pr 130:108–121

Candes EJ (2008) The restricted isometry property and its implications for compressed sensing. CR Math 346(9–10):589–592

Candes EJ, Fernandez-Granda C (2014) Towards a mathematical theory of super- resolution. Commun Pur Appl Math 67(6):906–956

Chae DH, Sadeghi P, Kennedy RA (2010) Effects of basis-mismatch in compressive sampling of continuous sinusoidal signals. 2010 2nd International Conference on Future Computer and Communication, IEEE.

Chen ZS, Sheng H, Xia YM, Wang WM, He J (2021) A comprehensive review on blade tip timing-based health monitoring: status and future. Mech Syst Signal Process 149:107330

Chi Y, Scharf LL, Pezeshki A, Calderbank AR (2011) Sensitivity to basis mismatch in compressed sensing. IEEE T Signal Process 59(5):2182–2195

Diamond S, Boyd S (2016) CVXPY: a python-embedded modeling language for convex optimization. J Mach Learn Res 17:2909–2913

Farrar CR, Worden K (2010) An introduction to structural health monitoring. Cism Courses Lect. https://doi.org/10.1007/978-3-7091-0399-9_1

Grieves M, Vickers J (2017) Digital twin: mitigating unpredictable, undesirable emergent behavior in complex systems. Transdisciplinary perspectives on complex systems. Springer, pp 85–113

Guo HT, Duan FJ, Zhang JL (2016) Blade resonance parameter identification based on tip-timing method without the once-per revolution sensor. Mech Syst Signal Process 66–67:625–639

He CB, Li H, Zhao XW (2018) Weak characteristic determination for blade crack of centrifugal compressors based on underdetermined blind source separation. Measurement 128:545–557

Joung KK, Kang SC, Paeng KS, Park NG, Choi HJ, You YJ, Von Flotow A (2006) Analysis of vibration of the turbine blades using non-intrusive stress measurement system. Proceedings of the ASME Power Conference, 391–397.

Karve PM, Guo YL, Kapusuzoglu B, Mahadevan S, Haile MA (2020) Digital twin approach for damage-tolerant mission planning under uncertainty. Eng Fract Mech 225:106766

Li YX, Chi YJ (2016) Off-the-grid line spectrum denoising and estimation with multiple measurement vectors. IEEE Trans Signal Proces 64(5):1257–1269

Li S, Yang DH, Tang GG, Wakin MB (2018) Atomic norm minimization for modal analysis from random and compressed samples. IEEE Trans Signal Proces 66(7):1817–1831

Li CF, She HX, Tang QS, Wen BC (2019) The coupling vibration characteristics of a flexible shaft-disk-blades system with mistuned features. Appl Math Model 67:557–572

Li Y, Wang X, Ding Z (2020) Multidimensional spectral super-resolution with prior knowledge with application to high mobility channel estimation. IEEE J Sel Areas Commun 38(12):2836–2852

Lin J, Hu Z, Chen ZS, Yang YM, Xu HL (2016) Sparse reconstruction of blade tip-timing signals for multi-mode blade vibration monitoring. Mech Syst Signal Pr 81:250–258

Liu ZB, Duan FJ, Niu GY, Ye DC, Feng JN, Cheng ZH, Fu X, Jiang JJ, Zhu J, Liu MR (2022) Reconstruction of blade tip-timing signals based on the MUSIC algorithm. Mech Syst Signal Process 163:108137

Mohamed ME, Bonello P, Russhard P (2019) A novel method for the determination of the change in blade tip timing probe sensing position due to steady movements. Mech Syst Signal Process 126:686–710

Mohamed ME, Bonello P, Russhard P (2020) An experimentally validated modal model simulator for the assessment of different blade tip timing algorithms. Mech Syst Signal Process 136:106484

Ritto TG, Rochinha FA (2021) Digital twin, physics-based model, and machine learning applied to damage detection in structures. Mech Syst Signal Process 155:107614

Russhard P (2010) Development of a blade tip timing based engine health monitoring system. The University of Manchester

Semper S, Romer F (2019) Admm for Nd line spectral estimation using grid-free compressive sensing from multiple measurements with applications to Doa estimation. 2019 IEEE International Conference on Acoustics, Speech and Signal Processing (ICASSP), 4130–4134.

Stephan C, Berthillier M, Lardies J, Talon A (2008) Tip-timing data analysis for mistuned bladed discs assemblies. Proc Asme Turbo Expo 2008 5:447–455

Tang GG, Bhaskar BN, Shah P, Recht B (2013) Compressed sensing off the grid. IEEE Trans Inform Theory 59(11):7465–7490

Tutuncu RH, Toh KC, Todd MJ (2003) Solving semidefinite-quadratic-linear programs using SDPT3. Math Program 95(2):189–217

Vercoutter, A., M. Berthillier, A. Talon, B. Burgardt and J. Lardies (2012) Estimation of turbomachinery blade vibrations from tip-timing data. 10th International Conference on Vibrations in Rotating Machinery, London, Sept.

Wagner M, Park Y, Gerstoft P (2021) Gridless DOA estimation and root-MUSIC for non-uniform linear arrays. IEEE Trans Signal Proces 69:2144–2157

Wang ZK, Yang ZB, Wu SM, Li HQ, Tian SH, Chen XF (2020) An improved multiple signal classification for nonuniform sampling in blade tip timing. IEEE Trans Instrum Meas 69(10):7941–7952

Wang WM, Chen K, Zhang XL, Li WB (2022) A novel method to improve the precision of BTT under rapid speed fluctuation conditions. Mech Syst Signal Process 177:109203

Wei D, Li H, Chen Y, Cao H, Fan Z, Li Y (2022) Development of blade tip timing signal simulator based on a novel model reduction method of bladed disks. J Sound Vibr. 534:117053

Witos M (2013) High sensitive methods for health monitoring of compressor blades and fatigue detection. Sci World J. 2013:1–31

Wong WK, Zhou JL (2019) CVX-based algorithms for constructing various optimal regression designs. Can J Stat 47(3):374–391

Wu XH, Zhu WP, Yan J (2018) A high-resolution doa estimation method with a family of nonconvex penalties. IEEE Trans Veh Technol 67(6):4925–4938

Wu SM, Zhao ZB, Yang ZB, Tian SH, Yang LH, Chen XF (2019) Physical constraints fused equiangular tight frame method for blade tip timing sensor arrangement. Measurement 145:841–851

Yang Z, Xie LH (2015) On gridless sparse methods for line spectral estimation from complete and incomplete data. IEEE Trans Signal Proces 63(12):3139–3153

Yang Z, Xie LH (2018) Frequency-selective Vandermonde decomposition of Toeplitz matrices with applications. Signal Process 142:157–167

Yang LH, Mao Z, Wu SM, Chen XF, Yan RQ (2021a) Steady-state coupling vibration analysis of shaft-disk-blade system with blade crack. Nonlinear Dynam 105(1):61–98

Yang LH, Yang ZS, Mao Z, Wu SM, Chen XF, Yan RQ (2021) Dynamic characteristic analysis of rotating blade with transverse crack-part I: modeling, modification, and validation. J Vib Acoust. https://doi.org/10.1115/1.4049385

Yang L, Mao Z, Wu S, Chen X, Yan R (2021c) Nonlinear dynamic behavior of rotating blade with breathing crack. Front Mech Eng 16(1):196–220

Yang LH, Mao Z, Chen XF, Yan RQ, Xie JS, Hu HF (2022) Dynamic coupling vibration of rotating shaft-disc-blade system—modeling, mechanism analysis and numerical study. Mech Mach Theor 167:104542